minerals

MDPI

Article

Stabilization of Mn^{4+} in Synthetic Slags and Identification of Important Slag Forming Phases

Alena Schnickmann [1,*], Danilo Alencar De Abreu [2], Olga Fabrichnaya [2] and Thomas Schirmer [1]

[1] Department of Mineralogy, Geochemistry, Salt Deposits, Institute of Disposal Research, Clausthal University of Technology, Adolph-Roemer-Str. 2A, 38678 Clausthal-Zellerfeld, Germany; thomas.schirmer@tu-clausthal.de
[2] Institute of Materials Science, TU Bergakademie Freiberg, Gustav-Zeuner Str. 5, 09599 Freiberg, Germany; danilo-alencar.de-abreu@iww.tu-freiberg.de (D.A.D.A.); olga.fabrichnaya@iww.tu-freiberg.de (O.F.)
* Correspondence: alena.schnickmann@tu-clausthal.de

Abstract: The expected shortage of Li due to the strong increase in electromobility is an important issue for the recovery of Li from spent Li-ion batteries. One approach is pyrometallurgical processing, during which ignoble elements such as Li, Al and Mn enter the slag system. The engineered artificial mineral (EnAM) strategy aims to efficiently recover critical elements. This study focuses on stabilizing Li-manganates in a synthetic slag and investigates the relationship between Mn^{4+} and Mg and Al in relation to phase formation. Therefore, three synthetic slags (Li, Mg, Al, Si, Ca, Mn, O) were synthesized. In addition to $LiMn^{3+}O_2$, $Li_2Mn^{4+}O_3$ was also stabilized. Both phases crystallized in a Ca-silicate-rich matrix. In the structures of Li_2MnO_3 and $LiMnO_2$, Li and Mn can substitute each other in certain proportions. As long as a mix of Mn^{2+} and Mn^{3+} is present in the slag, spinels form through the addition of Mg and/or Al.

Keywords: lithium–manganate (IV); lithium–manganate (III); engineered artificial minerals (EnAMs); synthetic slag; phase diagram

Citation: Schnickmann, A.; De Abreu, D.A.; Fabrichnaya, O.; Schirmer, T. Stabilization of Mn^{4+} in Synthetic Slags and Identification of Important Slag Forming Phases. *Minerals* **2024**, *14*, 368. https://doi.org/10.3390/min14040368

Academic Editor: Hugo Marcelo Veit

Received: 29 February 2024
Revised: 26 March 2024
Accepted: 28 March 2024
Published: 30 March 2024

1. Introduction

1.1. Recovery of Critical Elements from the Slag Phase

The usage of critically relevant elements, such as Li, will be increasingly in demand due to their use in various technological areas [1]. The EU has established a list of critical elements, which includes Li as well as Co [2]. In Li-ion batteries (LIBs), these two elements are used as cathode materials ($LiCoO_2$). The geological supply of such elements is limited, thus the recovery of, e.g., Li from the industrial waste stream. such as from old LIBs, is indispensable [3–5]. Pyrometallurgical processes [6] are a promising method for the recovery. With this route, various elements (e.g., Co, Ni or Cu) can be recovered directly, while base elements (e.g., Li, Mg, Al or Mn) are either lost as dust or enter the slag phase and form complex compounds. For efficient recovery of critical elements such as Li, it is essential to concentrate the element of interest in a single phase within the slag [1,7]. In addition, this phase should have a high Li-content as well as good processing properties (e.g., habitus, crystal size, magnetic properties). The stabilization of Li in a single phase for an efficient recovery of critically relevant elements is the idea behind engineered artificial minerals (EnAMs) [8] (Figure 1).

1.2. Potential EnAMs for Efficient Recovery

A study by Elwert et al. [9] shows that the Li-aluminate $LiAlO_2$ would be suitable as a potential EnAM, as the idiomorphic to hypidiomorphic crystals can be separated from the remaining slag via flotation [10]. In the presence of especially Mg, Al and Mn, spinel complexes are formed during solidification and solid solutions occurred between spinels (e.g., $MgMn_2O_4$, $MgAl_2O_4$, $MnAl_2O_4$ and $Mn^{2+}Mn^{3+}{}_2O_4$), which hampered the formation of $LiAlO_2$ [11–13]. In addition, this Li aluminate can contain up to 3 wt.%

Si, which complicates hydrometallurgical processing [10]. As the use of Mn in new Li batteries increases, Mn will become part of a complex slag system along with Li, Mg and Al. In addition, small amounts of Mg and Al in $LiMnO_2$ and Li_2MnO_3 are expected to promote intralayer diffusion and Mg should also promote interlayer diffusion [14]. For this reason, current research is focusing on the stabilization of Li in Li-manganates as a potential EnAM [8]. The difficulties here are the redox-sensitive behavior of Mn and the Jahn–Teller effect on the Mn^{3+} at temperatures above 1445 K [12,13]. Schnickmann et al. [8] showed that it is possible to stabilize a Li-manganate in a complex synthetic oxide slag system (Li, Mg, Al, Si, Ca, Mn). Under a normal atmosphere, a mixture between Mn^{2+} and Mn^{3+} was present and pure $LiMnO_2$ was formed. Nevertheless, the formation of spinels and spinel solid solutions could not be prevented, as well as the incorporation of Mn^{2+} into the Ca-silicate matrix. In a follow-up experiment, pure oxygen (100% O_2) was used to stabilize a higher Mn oxidation stage in the slag. For this experiment, the same batch precursors were used as in Schnickmann et al. [8]. This experiment is designed to investigate whether it is possible to stabilize higher Mn oxidation states in synthetic slags and whether Mn^{4+} forms a compound with the other elements, especially with Mg and/or Al.

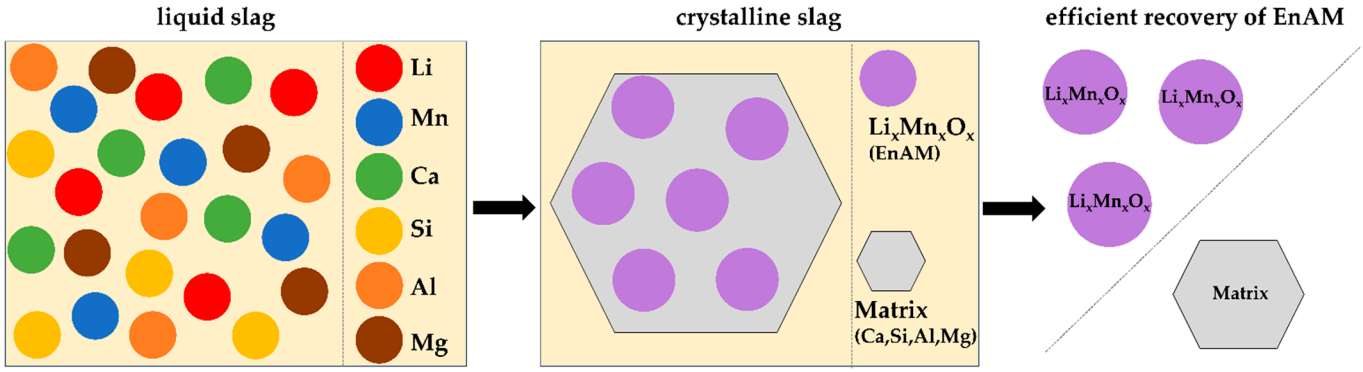

Figure 1. Sketch of the EnAM strategy for efficient Li recovery. The aim is to form a Li-manganate as an early crystallizate from the liquid melt. The other elements (Mg, Al, Si, Ca) should form matrix-forming phases. This early crystallizate (Li-Manganate) should be efficiently separated from the matrix.

1.3. Important Slag Forming Phases

In a complex slag system consisting of Li_2O, MgO, Al_2O_3, SiO_2, CaO and MnO, mainly binary and ternary oxide compounds are formed, followed by a residual melt [8]. The compounds described below represent possible phases in a crystalline slag with a special focus on Li-rich compounds and the Mn oxides. Compounds between Mn^{4+} and Al/Mg have not yet been described in the literature. The ternary compounds are of minor importance for the results presented and are therefore not discussed in detail in this chapter.

The Li_2O-MnO_x system ($1 \leq x \leq 2$) must be considered for the investigation of possible Mn-containing EnAMs. Due to the redox sensitivity of Mn, the formation of various Li-manganates with different concentrations and Mn speciations are possible. The phase equilibria in the Li_2O-MnO_x system in air is shown in Figure 2. According to the experimental data obtained by Paulsen and Dahn [15], cubic spinel transforms to tetragonal spinel at high temperatures. A miscibility gap between hausmannite (Mn_3O_4) and t-spinel was proposed. $LiMnO_2$ is stable at temperatures higher than 1223 K, while the Li_2MnO_3 phase is stable up to approximately 1240 K. In addition to Paulsen and Dahn [15], Longo et al. [16] also described such compounds in detail, as well as the influence of temperature, pressure and pH on the formation and stability of such Li-manganates. Below 400 °C, the cubic spinel phases with stoichiometry, $LiMn_{1.75}O_4$ and $Li_4Mn_5O_{12}$, are found to be stable. They can also be part of the spinel solid solution, as shown in the calculations of [17], but to achieve equilibrium at these low temperatures would be problematic. The phase $Li_2Mn_3O_7$ is calculated to be stable, but its stability has not yet been experimentally proven [15,16,18].

Between 400 and 800 °C, the Li-spinel ($Li_{(1+x)}Mn_{(2-x)}O_4$) has a large stability field between $LiMn_2O_4$ ($Mn^{3.5+}$) and $Li_4Mn_5O_{12}$ (Mn^{4+}) and can coexist with Li_2MnO_3 (Mn^{4+}). Above 800 °C, Li_2MnO_3 and $LiMn_2O_4$ decompose into Mn_3O_4 and O_2 alongside layered $LiMnO_2$. From 1000 to 1060 °C, orthorhombic $LiMnO_2$ can coexist with lithiated hausmannite ($Li_xMn_{3-x}O_4$) [15]. According to Mishra and Ceder [19], the Jahn–Teller distortion affects the tetragonal spinel $LiMn_2O_4$ as well as orthorhombic (e.g., $LiMnO_2$) and monoclinic layered structures [19]. In addition, the investigations by Schnickmann et al. [8] showed that in the $LiMnO_2$ system the Li and Mn contents can be exchanged and that this compound can incorporate up to 0.35 wt.% Al.

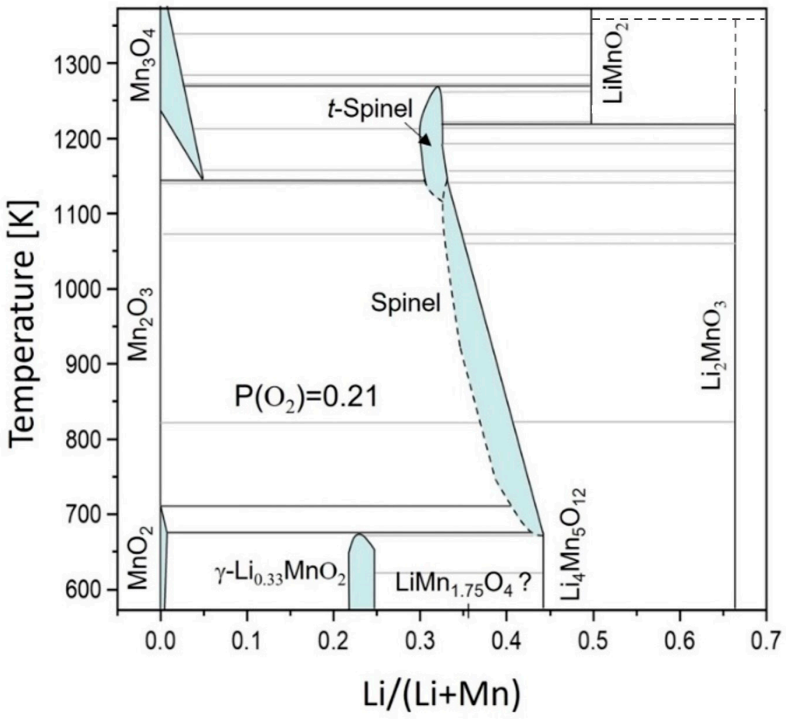

Figure 2. Adapted phase diagram of the Li_2O-MnO_x system in air based on experimental data obtained from Paulsen and Dahn [15].

Due to their good flotation properties, Li-aluminates have been investigated as potential EnAMs for a long time. Recently, thermodynamic assessments of the Li_2O-Al_2O_3 system using the CALPHAD approach have been published by Konar et al. [20] and De Abreu et al. [21]. Moreover, De Abreu et al. experimentally studied the phase equilibria in the Al_2O_3-rich part of the diagram and made calorimetric measurements of heat capacity for intermediate phases. The calculated phase diagram is shown in Figure 3a. Three stable intermediate phases were proposed: $LiAl_5O_8$, $LiAlO_2$ and Li_5AlO_4. $LiAlO_2$ has already been extensively analyzed and discussed for its potential as an EnAM [20,21]. Two polymorphs are reported for $LiAlO_2$: the low-temperature α-phase (trigonal) and the high-temperature γ-phase (tetragonal). Two stable modifications of $LiAl_5O_8$ with spinel structure but with different space groups were found in the alumina-rich side of the phase diagram. High-temperature modification of the spinel is inversed and stable with some homogeneity range. No evidence of $LiAl_{11}O_{17}$ was found in the microstructures and thus $LiAl_{11}O_{17}$ is not treated as stable.

Another important area of Li-rich phases is the Li_2O-SiO_2 system, with the following stable phases: $Li_2Si_2O_5$, Li_2SiO_3, Li_4SiO_4 and Li_8SiO_6 (ordered by decreasing Si concentration). According to the latest results, the $Li_6Si_2O_7$ phase is treated as metastable. Li_2SiO_3 is formed from a Li_2O-SiO_2-rich melt.

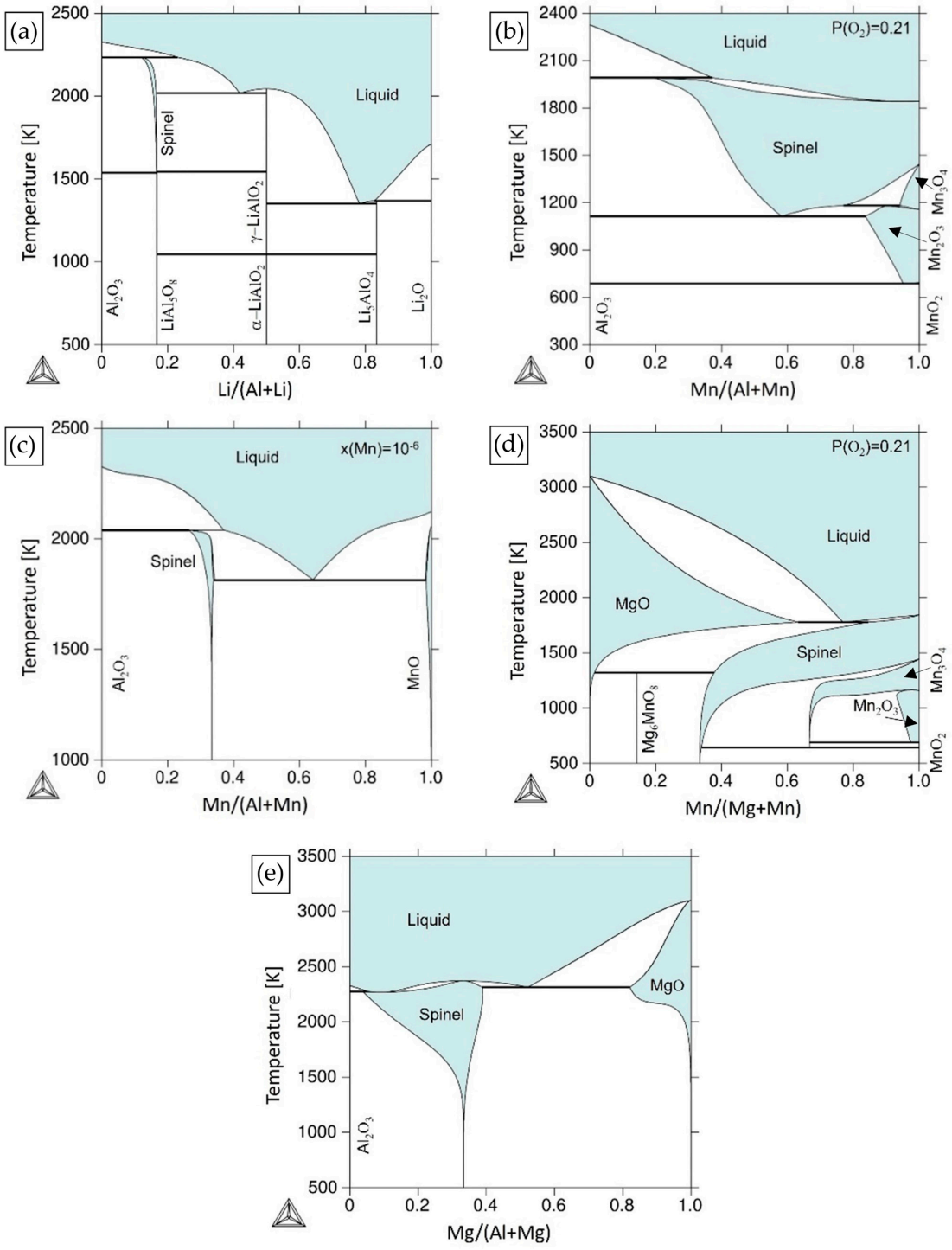

Figure 3. Calculated phase diagrams of the: (**a**) Li_2O-Al_2O_3 system, (**b**) Al_2O_3-MnO_x system in air; (**c**) Al_2O_3-MnO_x system in the presence of metallic Mn; (**d**) MgO-MnO_x system in air and (**e**) Al_2O_3-MgO system with the thermodynamic parameters optimized from [13,21–23].

Spinels are the most important Li-free compounds, whereas hausmannite ($Mn^{2+}Mn^{3+}{}_2O_4$) is the most important compound in the MnO-Mn_2O_3 system. Below 1172 °C, the Jahn–Teller effect has an influence on the Mn^{3+} position and causes deformation of the crystal parameters. The transformation from tetragonal to cubic is reversible and crystal lattice changes from cubic to tetragonal on cooling. Hausmannite can be regarded as a low-temperature phase as well as a deformed spinel under normal conditions (1 atm; 25 °C) and low oxygen partial pressure. Hausmannite forms from Mn_2O_3 at 1445 K and air oxygen partial pressure.

It can form solid solutions with other spinel compounds. One of the most important spinels in the MnO-Al_2O_3 system is galaxite ($MnAl_2O_4$) [12,13,20]. The calculated phase diagrams with thermodynamic parameters optimized by [13] for the Al_2O_3-MnO_x system in air and in the presence of metallic Mn are shown in Figure 3b,c, respectively. In the presence of metallic Mn, thus in varying oxygen partial pressure p(O_2) with temperature, the homogeneity range of the spinel phase is narrow and its stoichiometry is close to $MnAl_2O_4$. According to crystallographic data, the spinel phase is normal at low temperature, with tetrahedral sites occupied by Mn^{2+} cations, but with temperature increases the degree of inversion (fraction of Al^{3+} in tetrahedral sites) increases. According to calculations, which agree with experimental results, the homogeneity range of spinel extends with an increase in oxygen partial pressure and in air conditions (p(O_2) = 0.21 bar) the homogeneity range of the cubic spinel extends from Mn_3O_4 to $MnAl_2O_4$ (at high temperatures). It should be noted that the Mn_3O_4 spinel forming from Mn_2O_3 via oxygen release has a tetragonal structure. The tetrahedral sites are occupied by Mn^{2+} and the octahedral sites by Mn^{3+}. Tetragonal spinel transforms to cubic types at 1443 K, probably due to the disproportionation reaction $Mn^{3+} \rightarrow Mn^{2+} + Mn^{4+}$ to reduce the Jahn–Teller distortion caused by Mn^{3+}.

Phase diagrams of other important systems containing the spinel phase, like MgO-MnO_x and MgO-Al_2O_3 systems are also shown in Figure 3d,e, respectively. The thermodynamic parameters obtained by [22] and [23] were applied to calculate the phase relationships for these binary systems. It should be noted that spinels with tetragonal and cubic structures were found in the MgO-MnOx system. Tetrahedral spinel has a homogeneity range from Mn_3O_4 to $MgMn_2O_4$, while cubic spinel extends from Mn_3O_4 to Mg_2MnO_4.

2. Materials and Methods

2.1. Chemicals and Preparation of Precursors and Reference Materials

For the melting experiment, the same batch of precursors was used as in the study by Schnickmann et al. [9], with the following chemical compositions: $LiNO_3$, $Mg(NO_3)_2 \times 6\ H_2O$, $Al(NO_3)_3 \times 9\ H_2O$, Köstrosol® 0830 AS, $Ca(NO_3)_2 \times 4\ H_2O$, $Mn(NO_3)_2 \times 4\ H_2O$ and $C_6H_8O_7$.

The gel-combustion method was used to prepare the precursors. For this purpose, common procedures [24,25] were adapted to the experimental setup in the laboratory. The method has also been described by Schnickmann et al. [8]. The gel-combustion product was thermally treated with NH_4NO_3 in quartz crucibles up to 480 °C (10 °K/min; Nabertherm LE 1/11/R7, Nabertherm GmbH, Lilienthal, Germany) to remove the residual carbon. In Table 1, the elemental composition of the precursors can be found.

Table 1. Elemental composition of the precursors in wt.% and at.%. The precursors have the same composition as [8].

	Precursor 1		**Precursor 2**		**Precursor 3**	
Element	wt.%	at.%	wt.%	at.%	wt.%	at.%
Li	1.9	6.3	1.9	6.3	1.8	5.8
Mg	0.0	0.0	1.2	1.1	1.2	1.1
Al	0.0	0.0	0.0	0.0	1.1	0.9
Si	19.3	15.9	19.1	15.6	18.9	15.4
Ca	29.9	17.2	29.4	16.9	29.0	16.7
Mn	9.8	4.1	9.2	3.9	8.6	3.7
O	39.1	56.4	39.2	56.2	39.4	56.4
Total	100.0	100.0	100.0	100.0	100.0	100.0

2.2. Melting Program

For the melting experiment, the thermally treated precursors were melted in Pt/Rh crucibles (filling capacity: 15 mL) under pure oxygen atmosphere at 200 L per hour in a chamber furnace (Nabertherm HT16/17, Nabertherm GmbH, Lilienthal, Germany).

The melt program of Schirmer et al. [10] and Schnickmann et al. [8] was adapted for this process (Figure 4). For each experiment, 1.20 g of sample material was used. The powder was not pressed or compacted in the crucible. All three samples were melted together in one run, in different crucibles, to achieve consistent conditions.

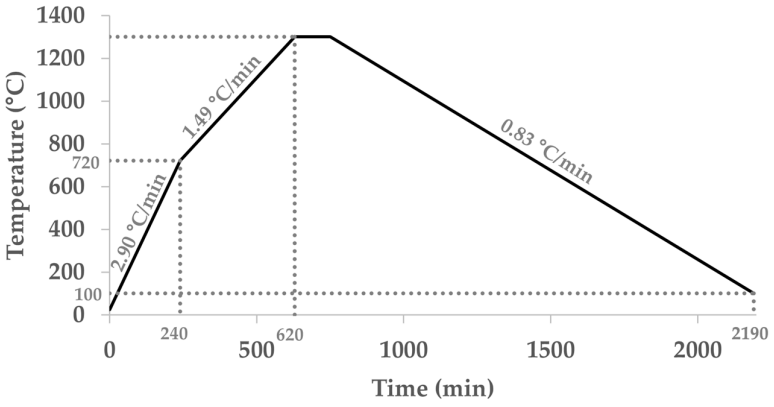

Figure 4. The heating program used for the experiments. Slow heating of the precursor (2.90 °C/min; 1.49 °C/min) should minimize the loss of Li. By cooling down more slowly, the phases should have enough time to form crystals that are as large as possible. During the entire melting experiment, the oxygen supply was 200 L/h.

Due to the reaction-resistant material, no reaction took place between the slag and the crucible. However, not all of the slag material could be removed from the crucible, resulting in the loss of small amounts. For example, 1.03 g of S1, 1.01 g of S2 and 1.05 g of S3 were present after the melting experiment. The areas of slag near the surface took on a reddish color, while the rest of the slag was dark gray to black. EPMA was used to analyze the near-surface samples and the remaining slag, which is representative of the entire slag.

2.3. Characterization Techniques

The mineralogical composition of the slags was quantitatively and qualitatively identified using powder X-ray diffraction (PXRD) and electron probe microanalysis (EPMA).

The crystalline phases in the slag sample were analyzed using PXRD (Panalytical X-Pert Pro Diffractometer, Malvern Panalytical GmbH, Kassel, Germany). For the measurement (2θ-angle range from 5° to 100°; step size 0.0066°; 150.45 s per step), a Co-X-ray tube (Malvern Panalytical GmbH, Kassel, Germany, λ = 1.7902 Å, 40 kV, 40 mA) was used. The individual crystalline phases were classified via the American Mineralogist Crystal Structure Database [26] and the pdf-2 ICCD XRD database [27].

The elemental composition of single grains/crystals in the prepared thin sections were determined with EPMA (Cameca SXFIVE FE Field Emission, CAMECA SAS, Gennevilliers Cedex, France) using the Kα lines (Mg, Al, Si, Ca, Mn). For the measurement (15 kV beam diameter 100–600 nm; Schottky type [28]), the device was calibrated beforehand with certified reference materials (CRM: P&H Developments Ltd.; Glossop, Derbyshire, UK and Astimex Standards Ltd.; Toronto, ON, Canada). The measured intensities of the emitted X-rays were evaluated using the X-PHI model [29]. With the chosen method, the Li content cannot be analyzed quantitatively with the required precision. Therefore, the element concentration of Li was determined using virtual compounds according to T. Schirmer [30].

In order to validate the measurement method and obtain consistent results, repeated measurements were carried out on different days using the international standard rhodonite ($MnSiO_3$; Astimex). The low standard deviation (0.03) of Mn indicates that this element content can be analyzed very precisely and is suitable for calculating the Li content via virtual compounds (Table 2).

Table 2. The CRM rhodonite was used to verify the measurement accuracy of Mn. The Mn content can be determined with an inaccuracy of ±0.03%. Indication in wt.%. * The iron content was not measured.

Wt.%	Average Rhodonite	%StDev. Rhodonite	Ref. Rhodonite
MgO	1.92	0.01	2.0
Al_2O_3	0.011	0.002	n.a.
SiO_2	46.76	0.06	46.8
CaO	4.74	0.04	4.6
MnO	42.30	0.03	42.3
FeO *	4.34	n.a.	4.3

3. Results

3.1. PXRD

In all three samples, wollastonite ($CaSiO_3$; ICDD PDF2: 01-084-0654), as well as the Li-manganates $LiMnO_2$ (ICDD PDF2: 00-035-0749) and Li_2MnO_3 (ICDD PDF2: 01-081-1953) could be detected with PXRD. Rankinite ($Ca_3Si_2O_7$; ICDD PDF2: 01-076-0623) was detected in slags 1 and 2 and larnite (Ca_2SiO_4; ICDD PDF2: 00-029-0369) in slag sample 3. The presence of hausmannite ($Mn^{2+}Mn^{3+}{}_2O_4$; ICDD PDF2 00-024-0734) and the Li-silicate Li_2SiO_3 (ICDD PDF2: 00-029-0828) is conceivable. However, the presence of these two phases cannot be clearly verified with this method due to line overlaps. Schnickmann et al. [8] have already discovered that within the Li-manganate $LiMnO_2$, the elements Li and Mn can replace each other, which can result in shifting to smaller or larger lattice parameters. The same applies to the replacement of Mn^{2+} in Ca-silicate matrices. An exchange of elements in the crystal lattice is only possible as long as the exchangeable elements have approximately the same ionic radii (e.g., [31]). An overview of the recorded diffractograms of the three slags is given in Figure 5.

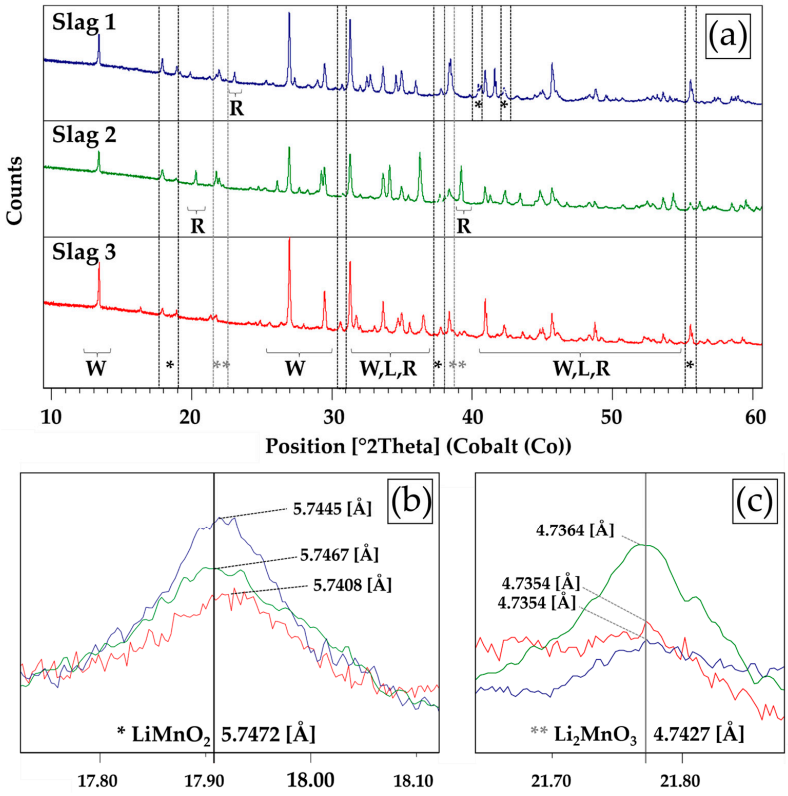

Figure 5. (**a**) Recorded PXRD pattern of the three slag samples. The identified main phases wollastonite (W), rankinite (R), larnite (L), $LiMnO_2$ (*) and Li_2MnO_3 (**) were marked. (**b**) Identified $LiMnO_2$ reflex in the slag samples (S1–S3). (**c**) Identified Li_2MnO_3 reflex in the slag samples (S1–S3).

3.2. EPMA

With EPMA, the following phases were determined:

- $Li_{(1-x)}Mn_{(1+0.33x)}O_2$ / $Li_{(1+x)}Mn_{(1-0.33x)}O_2$ (slags 1, 2, 3)
- $Li_{(2-x)}Mn_{(1+0.33x)}O_3$ / $Li_{(2+x)}Mn_{(1-0.33x)}O_3$ (slag 2)
- Li_2SiO_3 (slags 1, 2)
- $Li_xMn_{(3-x)}O_4$ (slags 1, 2, 3)
- $CaSiO_3$ (slags 1, 2, 3)
- $Ca_3Si_2O_7$ (slags 1, 2)
- Ca_2SiO_4 (slag 3)
- Residual melt (slags 2, 3)

These phases were identified based on the elemental content of the individual grains (point measurements, line scans) and the crystal shape. The crystal shape provides additional information regarding the processes during solidification (Figure 6).

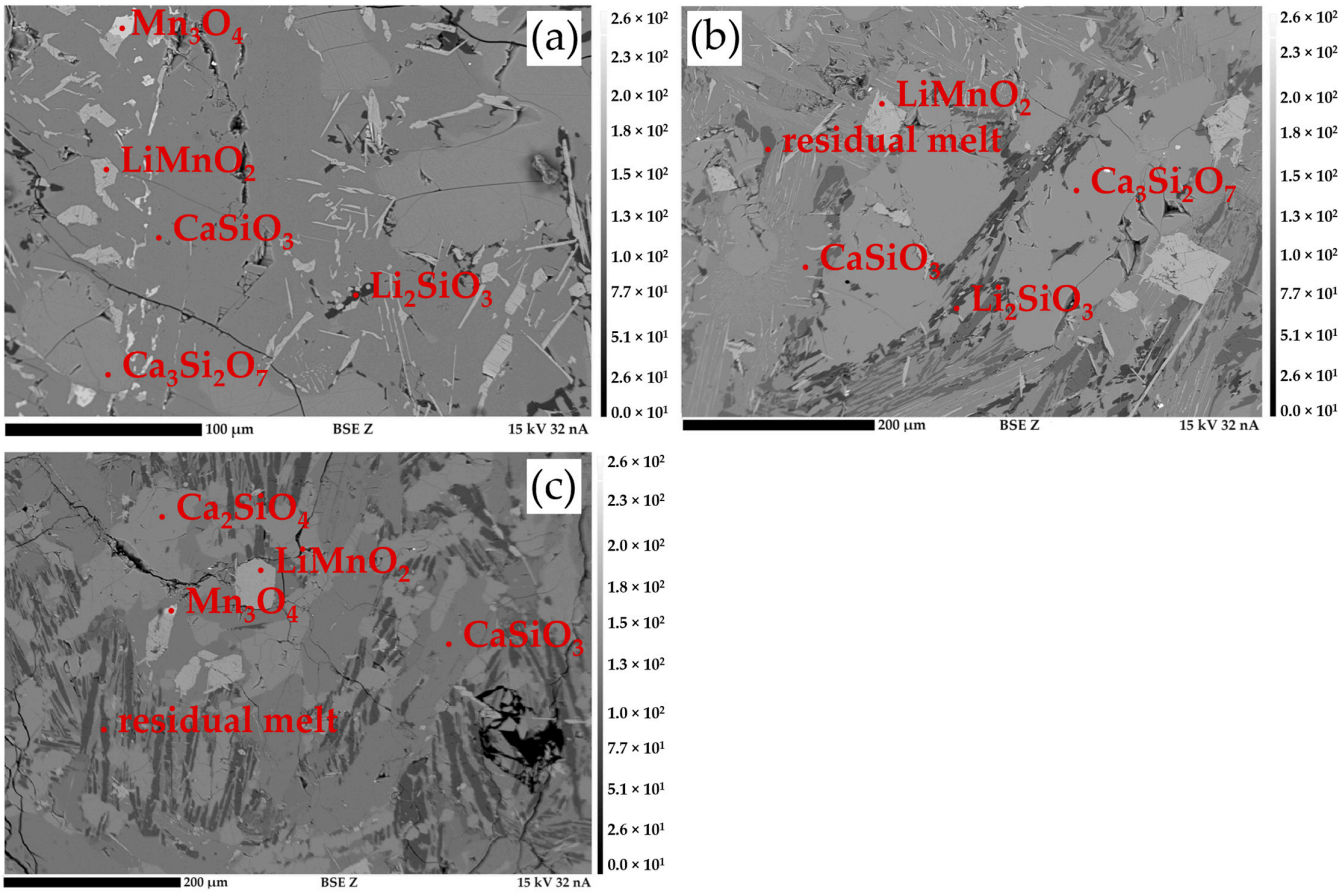

Figure 6. Recorded BSE(Z) micrographs of the three slags. In light gray: hausmannite (Mn_3O_4); medium gray: Li-manganate ($LiMnO_2$); dark gray: wollastonite ($CaSiO_3$) and rankinite ($Ca_3Si_2O_7$)/larnite (Ca_2SiO_4). (**a**) S1; (**b**) S2; (**c**) S3.

3.2.1. Li-Manganates

Two different Li-manganates ($Li_2Mn^{4+}O_3$ and $LiMn^{3+}O_2$) were found in the slag samples. Li_2MnO_3 was only detected via EPMA in slag 2 in a prepared, near-surface region of the slag where 2 wt.% Mg was added. This phase theoretically contains 47.03 wt.% Mn and 11.88 wt.% Li. Within this phase, the average measured Mn content was 47.08 wt.% (min.: 46.88 wt.%; max.: 47.28 wt.%) (Figure 7). In addition, this phase forms idiomorphic crystals between 30 and 100 µm. Based on the crystal shape, it can be determined that Li_2MnO_3 forms early during solidification. Point measurements and recorded line scans

within this phase show that no other elements (e.g., Mg, Ca, Si) have been incorporated. According to the line scan results, the Mn content within the crystal is constant (Figure 8).

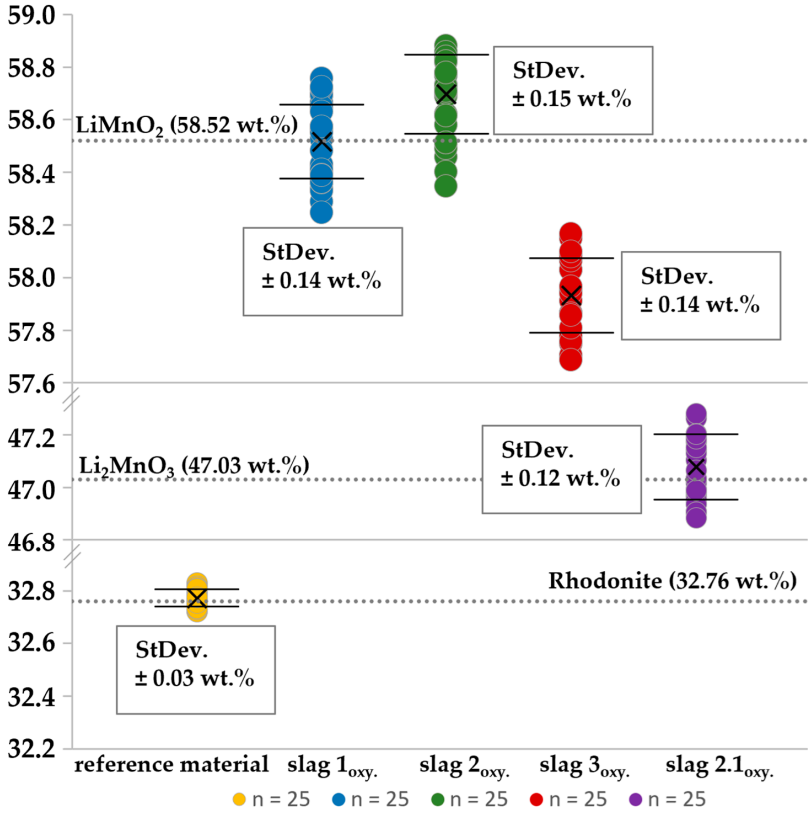

Figure 7. Overview of the measured Mn concentrations within the Li-manganates in the three slags. The dotted lines indicate the Mn concentrations of the pure stoichiometric compounds. In all three slag samples, the phase $LiMnO_2$ was found; Li_2MnO_3 was only found in slag 2 (2.1). The results shown are based on point measurements in different crystals of the respective phase. Measurements on the reference material rhodonite demonstrate that the Mn content can be measured with an accuracy of ±0.03%. X marks the mean value.

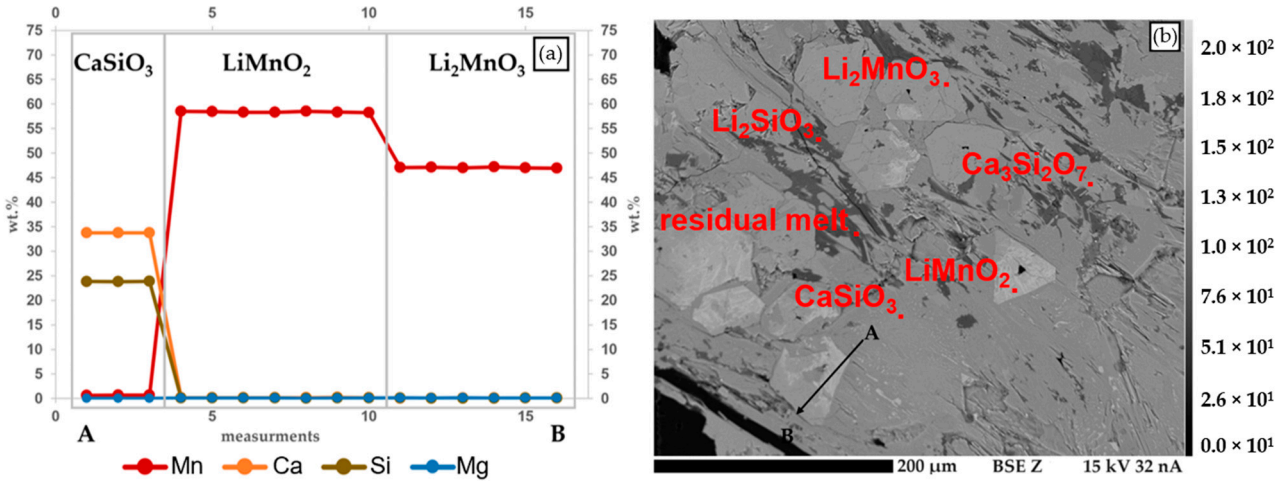

Figure 8. Elemental composition of the matrix ($CaSiO_3$) and the two Li-manganates (Li_2MnO_3) and ($LiMnO_2$) in slag 2. (**a**) The line scan results show that minimal amounts of Mn^{2+} were incorporated into the matrix. Furthermore, there is no decrease or increase in the element distribution towards the grain boundaries. (**b**) BSE(Z) image showing the path of the line scan (A: start, B: end, step size: 5.3 µm).

The crystallized $LiMnO_2$ formed idiomorphic to partially hypidiomorphic crystals with an average size of 50 µm. In addition, elongated $LiMnO_2$ needles crystallized in the Ca-silicate matrix. In theory, this phase contains 58.52 wt.% Mn and 7.39 wt.% Li. Within the slag, the average Mn content in S1 was 58.52 wt.% (min.: 58.25 wt.%; max.: 58.76 wt.%), in S2 it was 58.67 wt.% (min.: 58.35 wt.%; max.: 58.88 wt.%) and in S3 it was 57.88 wt.% (min.: 57.02 wt.%; max.: 58.17 wt.%) (Figure 8). Slag 3 contains 0.83 wt.% Al, which results in a lower Mn concentration (Table 3). The results of the line scans show that the Mn content within the individual grains is almost homogeneous. In addition, no decrease in element concentration is observed towards the grain boundaries (Figure 9).

Table 3. For the two Li-manganates $LiMnO_2$ and Li_2MnO_3, the average structural formula was calculated from all measuring points. To clarify the possible exchange of Li and Mn ions in the crystal lattice, a structural formula was also calculated for the lowest and highest Mn concentration according to: $Li_{(1-x)}Mn_{(1+0.33x)}O_2$ / $Li_{(1+x)}Mn_{(1-0.33x)}O_2$ and $Li_{(2-x)}Mn_{(1+0.33x)}O_3$ / $Li_{(2+x)}Mn_{(1-0.33x)}O_3$.

Sample	$LiMnO_2$ (Average)	$LiMnO_2$ (min.)	$LiMnO_2$ (max.)
S1 (n = 25)	$Li^{1+}_{1.0}Mn^{3+}_{1.0}O_2$	$Li^{1+}_{1.01}Mn^{3+}_{0.99}O_2$	$Li^{1+}_{0.98}Mn^{3+}_{1.01}O_2$
S2 (n = 25)	$Li^{1+}_{1.0}Mn^{3+}_{1.0}O_2$	$Li^{1+}_{1.01}Mn^{3+}_{1.00}O_2$	$Li^{1+}_{0.97}Mn^{3+}_{1.01}O_2$
S3 (n = 25)	$Li^{1+}_{1.0}(Mn^{3+}_{0.97}Al^{3+}_{0.03})O_2$	$Li^{1+}_{1.02}(Mn^{3+}_{0.96}Al^{3+}_{0.03})O_2$	$Li^{1+}_{0.96}(Mn^{3+}_{0.99}Al^{3+}_{0.02})O_2$
Sample	Li_2MnO_3 (average)	Li_2MnO_3 (min.)	Li_2MnO_3 (max.)
S2 (n = 25)	$Li^{1+}_{2.0}Mn^{3+}_{1.00}O_3$	$Li^{1+}_{2.02}Mn^{3+}_{0.99}O_3$	$Li^{1+}_{1.97}Mn^{3+}_{1.01}O_2$

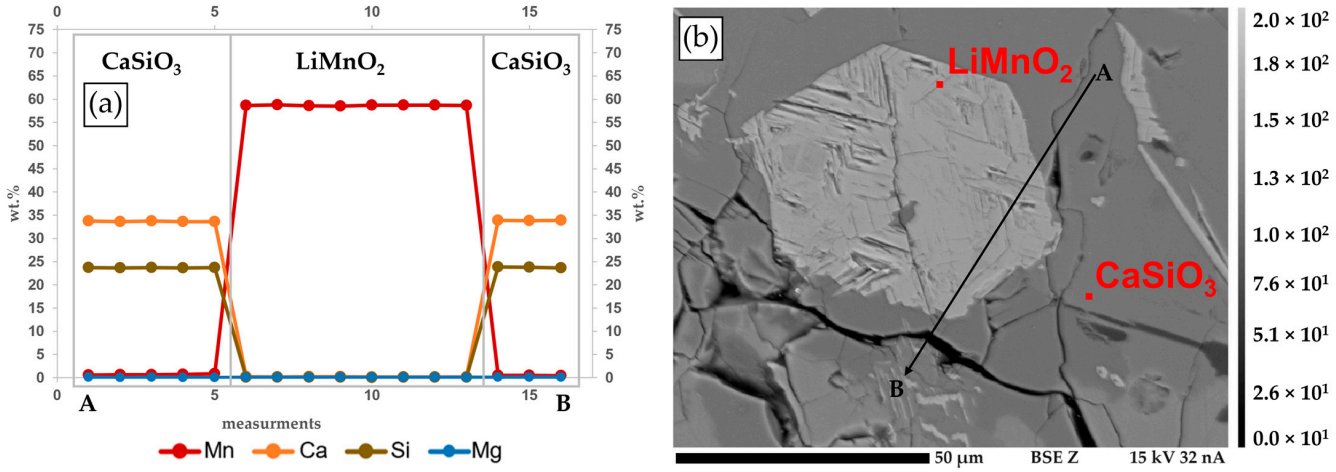

Figure 9. Elemental composition of the matrix ($CaSiO_3$) and Li-manganate (III) ($LiMnO_2$) in slag 2. (**a**) The line scan results show that minimal amounts of Mn^{2+} were incorporated into the matrix. Furthermore, there is no decrease or increase in the element distribution towards the grain boundaries. (**b**) BSE(Z) image showing the path of the line scan (A: start, B: end, step size: 4.4 µm).

3.2.2. Hausmannite and Spinel

Lithium-rich hausmannite was found in all three slag samples. Hausmannite consists of a mixture of Mn^{2+} and Mn^{3+} occupying tetrahedral and octahedral sites, respectively. When Mn^{2+} is substituted by Li^{1+}, Mn^{4+} can appear in the octahedral sublattice to balance the charge without a change in oxygen stoichiometry. However, there is not enough crystallographic data for the site occupancies of delithiated hausmannite. Additionally, tetragonal Mn_3O_4 and orthorhombic $LiMnO_2$ are intergrown. With an average crystal size of 10–30 µm, these crystals are significantly smaller than $LiMnO_2$. In all three slag samples, the incorporation of other elements into the crystal lattice was detected. The incorporation of Li was recorded in all slag samples. The largest amount of Li was incorporated into S1, with 1.59 wt.%, followed by S2 with 0.80 wt.% and S3 with 0.51 wt.%. In addition, an average incorporation of 0.84 wt.% Mg and 0.82 wt.% Al was observed in S3. For the

calculation of the spinel solid solution in S3, the following virtual compounds were defined: Mn_3O_4, $MnAl_2O_4$, $MgAl_2O_4$ and $Li_2Mn_2O_4$. This solid solution can be expressed by the following generalized stoichiometric formula: $(Li_{(2x)},Mg_{(x)},Mn_{(1-2x)})_{1+x}(Al_{(2-z)},Mn^{3+}{}_{(z)})_2O_4$. For Li-rich hausmannite in S1 and S2, the following generalized stoichiometric formula was applied: $(Li_{(2x)}Mn_{(1-x)})_{1+x}(Mn^{3+})_2O_4$ (Table 4).

Table 4. Determined structural formula of lithiated hausmannite in slags 1,2 and 3.

Sample	$Mn^{2+}Mn^{3+}{}_2O_4$
S1 (n = 12)	$(Li^{1+}{}_{0.50}Mn^{2+}{}_{0.75})Mn^{3+}{}_{2.0}O_4$
S2 (n = 16)	$(Li^{1+}{}_{0.26}Mn^{2+}{}_{0.87})Mn^{3+}{}_{2.0}O_4$
S3 (n = 16)	$(Li^{1+}{}_{0.16}Mn^{2+}{}_{0.84}Mg^{2+}{}_{0.08})(Mn^{3+}{}_{1.93}Al^{3+}{}_{0.07})O_4$

3.2.3. Li-Silicate

The Li-silicate Li_2SiO_3 was only found in S1 and S2. This phase forms 20 to 50 µm, rounded, elongated- to needle-shaped crystals. The hypidiomorphic to xenomorphic crystal shape indicates crystallization towards the end of solidification. The ideal crystals of this phase contain an average Si content of 31.22 wt.% and an average Li content of 15.43 wt.%. In S1, the average Si content is 31.66 wt.% and in S2 it is 31.68 wt.%. A higher Si content indicates a lower Li content.

3.2.4. Matrix-Forming Phases

The main matrix-forming mineral is wollastonite ($CaSiO_3$), followed by rankinite ($Ca_3Si_2O_7$) in S1 and S2 and larnite (Ca_2SiO_4) in S3. All three phases form xenomorphic crystals, which indicates crystallization at the end of solidification. Due to the approximately equal ionic radii of Mg^{2+}, Ca^{2+} and Mn^{2+}, Ca can be replaced by Mg and Mn in the crystal lattice [31]. In S1, 0.85 wt.% Mn was incorporated in wollastonite and 1.28 wt.% was incorporated in rankinite; in S2, there was 0.59 wt.% Mn in wollastonite and 2.22 wt.% in rankinite; in S3, there was 0.75 wt.% Mn in wollastonite and 6.97 wt.% Mn and 0.76 wt.% Mg in larnite (Table 5).

Table 5. Calculated structural formulas for the matrix-forming phases wollastonite ($CaSiO_3$) and rankinite ($Ca_3Si_2O_7$) in S1 and S2 and of larnite (Ca_2SiO_4) in S3.

Sample	$CaSiO_3$
S1 (n = 40)	$(Ca^{2+}{}_{0.99}Mn^{2+}{}_{0.02})Si^{4+}{}_{0.99}O_3$
S2 (n = 35)	$(Ca^{2+}{}_{0.99}Mn^{2+}{}_{0.01})Si^{4+}{}_{1.0}O_3$
S3 (n = 30)	$(Ca^{2+}{}_{0.99}Mn^{2+}{}_{0.02})Si^{4+}{}_{1.0}O_3$
Sample	$Ca_3Si_2O_7$
S1 (n = 40)	$(Ca^{2+}{}_{2.96}Mn^{2+}{}_{0.07})Si^{4+}{}_{1.99}O_7$
S2 (n = 40)	$(Ca^{2+}{}_{2.86}Mn^{2+}{}_{0.12}Mg^{2+}{}_{0.02})Si^{4+}{}_{2.0}O_7$
Sample	Ca_2SiO_4
S3 (n = 28)	$(Li^{1+}{}_{0.33}Ca^{2+}{}_{1.63}Mn^{2+}{}_{0.14}Mg^{2+}{}_{0.05})Si^{4+}{}_{0.99}O_4$

4. Discussion

The aim of this study was to investigate the stabilization of Mn^{4+} in the slag and to also verify which Li-rich phases are formed. Moreover, it should be investigated whether Mn^{4+} forms a compound with Mg or Al. Based on the phase diagrams, the experiment provides an overview of which phases crystallize in a synthetic slag consisting of Li_2O, MgO, Al_2O_3, SiO_2, CaO and MnO_x.

4.1. Influence of Mg and Al on Mn^{4+}

As can be seen from Figure 3e, the spinel phase in the MgO-Al_2O_3 system is the stable phase from low temperatures and has an extension towards both Al_2O_3 and MgO concentrations at high temperatures. The addition of MgO together with Al_2O_3 will increase the stability range of cubic spinel in the Li_2O-MnO_x-MgO-Al_2O_3 system.

The tetragonal-to-cubic transformations for the spinel phase in the MgO-MnO_x and Al_2O_3-MnO_x systems are driven by the Jahn–Teller distortion of octahedral sites, primarily occupied by Mn^{3+} ions. In the cubic phase, assuming a disproportionation of Mn^{3+} into Mn^{4+} and Mn^{2+} and the occupation the octahedral sites by Mn^{4+} and distribution of Mn^{2+} between tetrahedral and octahedral sites, a general formula for cubic spinel $(Al^{3+}, Mn^{2+})_1(Al^{3+}, Mn^{3+}, Mn^{2+}, Mn^{4+}, Va)_2(Mn^{2+}, Va)_2(O^{2-})_4$ is employed in the Al_2O_3-MnO_x system and $(Mg^{2+}, Mn^{2+})_1(Mg^{2+}, Mn^{3+}, Mn^{2+}, Mn^{4+}, Va)_2(Mg^{2+}, Mn^{2+}, Va)_2(O^{2-})_4$ in the MgO-MnO_x system. This formulation accommodates the variation in oxidation states of Mn within the crystal lattice. The cubic spinel phase is further characterized by the inclusion of vacancies (Va) on the octahedral sites and Mn^{2+}/Mg^{2+} in the interstitial site. The vacancies are introduced into the spinel model to extend the homogeneity ranges towards the Al_2O_3 side and interstitial site to model extension towards the MnO_x/MgO side. The applied models account for deviations from a perfectly ordered structure to describe the disordering in cationic sites and to describe the homogeneity ranges of spinel, thus enhancing the model applicability in a large range of conditions (compositions, temperature, oxygen partial pressure). The modeling of tetragonal spinel differs from that for cubic spinel by introducing Mn^{3+} into the tetrahedral site and via the absence of Mn^{4+} in the octahedral site in both systems. The tetragonal phase is stable at lower temperatures and in a more narrow composition range than cubic spinel.

The octahedral sites are substantially occupied by Mn^{4+} in cubic spinel in the MgO-MnO_x system in the whole possible composition range. A low concentration of Mn^{4+} is found in the spinel phase, with compositions close to stoichiometric $MnAl_2O_4$ in the Al_2O_3-MnO_x system even at high oxygen partial pressures. Thus, the introduction of Mg into the spinel phase not only enhances the stability but also effectively increases the Mn^{4+} concentration. This suggests a more pronounced role for Mg in maintaining the desired Mn oxidation state within the spinel structure.

The Li addition introduces a notable impact on the Mn^{4+} ion concentration on the octahedral sites. Substitution of Mn^{2+} for Li^{1+} in the tetrahedral sites reduces the charge of cations in spinel. In order to preserve the electroneutrality of this structure, the fraction of Mn^{4+} in the octahedral sites occupied by Mn^{3+} in tetragonal spinel should be increased. The increase in Mn^{4+} in octahedral sites should also reduce the Jahn–Teller effect caused by the electronic structure of the Mn^{3+} cation. It should be noted that in the stoichiometric spinel $LiMn_2O_4$, the cation Li^{1+} completely occupies the tetrahedral site and the ratio of Mn^{4+}/Mn^{3+} in octahedral site is equal to one. In cases where the Li content is higher than in stoichiometric spinel, Li^{1+} partially occupies octahedral site and ratio Mn^{4+}/Mn^{3+} becomes larger than one. With a temperature increase, the spinel becomes enriched by Mn, with a shift of composition to the stoichiometric spinel $LiMn_2O_4$ and an even higher content of Mn. Therefore, spinel with a high Li content is stable at lower temperatures and with a temperature increase it will decompose to spinel with a lower Li content and a Li_2MnO_3 phase (Figure 2). At a temperature of 1230 K, $LiMnO_2$ forms from spinel and Li_2MnO_3 and, at temperatures of 1250 K, Li_2MnO_3 decomposes into $LiMnO_2$ and Li_2O. Tetragonal spinel with a composition close to the stoichiometric one is stable in equilibrium with hausmannite with a much lower Li content from one side and from other side it is in equilibrium with $LiMnO_2$. The high-temperature stability limit of tetragonal spinel is defined by decomposition to hausmannite and $LiMnO_2$ at 1270 K.

According to the phase diagram shown in Figure 3b, no reactions should take place between MnO_2 and Al_2O_3 up to 688 K. The experimental results indicate that Mg and Al react to form spinel (Mg_2AlO_4) and therefore small amounts of these elements are not a problem for Li-manganate ($LiMnO_2$ or Li_2MnO_3) forming processes. As long as Mn^{2+} and

Mn^{3+} are present in the slag, spinels with Mg, Al and Mn are formed, which can interfere with the formation of EnAMs. In order to produce large and pure EnAM crystals that can also be efficiently separated from the rest of the slag, it must be ensured that $LiMnO_2$ or Li_2MnO_3 crystallize out of the melt first.

4.2. Li-Rich Phases as a New Potential EnAM

A total of four Li-containing phases crystallized out in the slag. These phases include the two Li-manganates $LiMnO_2$ and Li_2MnO_3, as well as the Li-silicate Li_2SiO_3 and the Li-containing hausmannite. With an average of 0.51 wt.% (S3) to 1.59 wt.% Li (S1), the Li content in hausmannite is too low to be a potential EnAM. The Li^{1+} is incorporated at the tetrahedral site and replaces Mn^{2+} in the crystal lattice. The incorporation of Li^{1+} into cubic $LiMn_2O_4$ can occur by balancing Mn^{4+} on the octahedral site, but it can also occur by deviation from the stoichiometry of oxygen by introducing vacancies [32–34]. There is not enough crystallographic data for hausmannite showing how substitution of Mn^{2+} by Li^{1+} is compensated. Since it is not possible to detect small amounts of Mn^{4+} with EPMA, more advance techniques should be used to further investigate whether Mn^{4+} can be incorporated into the crystal lattice of hausmannite for charge compensation. Hausmannite forms in addition to relatively tiny crystals and only occurs in small amounts. Due to the partially inhomogeneous mixture of Mn^{2+} and Mn^{3+} in this phase, further processing would be necessary after successful separation from the slag. With an average of 15.43 wt.% Li, Li_2SiO_3 would be more suitable as a new EnAM. However, this phase crystallizes towards the end of solidification and thus forms relatively small and needle-shaped crystals that are inhibitors for a successful separation of Li. Furthermore, Li and Si must be separated from each other after the recycling step. Therefore, Li-manganates like $LiMnO_2$ or Li_2MnO_3 would be more suitable as new potential EnAMs. The Li-manganate Li_2MnO_3, with 11.88 wt.% Li, could only be found in slag 2 where 2 wt.% Mg was added. No incorporation of other elements could be observed within this phase. As shown in Figure 2, the Li_2MnO_3 phase is stoichiometric, which corroborates with the absence of the solubility of other elements. Furthermore, the Li_2MnO_3 phase has some advantages as a new EnAM. Firstly, it is an early crystallite with large, idiomorphic crystals that contains more Li than $LiAlO_2$ (10.35 wt.% Li). The stabilization of only Mn^{4+} in the slag has the additional advantage that spinel formation with Mn could be suppressed and that the Jahn–Teller effect does not cause deformation. In addition, $LiMnO_2$ (7.39 wt.% Li) can also be considered as a potential EnAM. The low incorporation of Al (0.83 wt.%) does not seem to have any effect on the crystal lattice. According to Kong et al. [14], small amounts of Al in the Li-rich cathode material should promote intralayer diffusion.

Nevertheless, it remains to be determined which of the two Li manganates, $LiMnO_2$ or Li_2MnO_3, formed first. It is possible that $LiMnO_2$ forms first as a high-temperature phase and remains stable during cooling. At low temperatures, according to phase diagram, the stable phases are spinel and Li_2MnO_3. The alternative would be that Li_2MnO_3 forms first and decomposes to $LiMnO_2$ and Li_2O, which reacts with SiO_2 forming Li_2SiO_3.

5. Conclusions and Outlook

The presented results indicate that it was possible to stabilize the Mn^{4+}-containing Li-manganate Li_2MnO_3 in a synthetic slag, next to $LiMnO_2$. Both Li-manganates, Li_2MnO_3 and $LiMnO_2$, have proven to be extremely pure phases. Using EPMA for phase identification, $LiMnO_2$ was found in all areas of the prepared slag, while Li_2MnO_3 was found in only one area, the near-surface area of the slag that was affected by oxygen. Accordingly, based on the literature data for other slag systems, it is assumed that the added oxygen only affects the near-surface region due to the low viscosity of the melt [35,36]. In addition, it needs to be clarified which elements can be added to the system to reduce the viscosity. For this purpose, future experiments should investigate whether, as described in the literature (e.g., [37]), the viscosity can be reduced by adding FeO and Fe_2O_3 so that the oxygen can affect the entire melt, with the aim of stabilizing Mn^{4+} throughout the slag. Stabilization of

Mn^{4+} could provide further important experimental data on whether spinel formation can be prevented or whether Mn^{4+} from compounds with elements other than Li.

However, the conditions under which Li_2MnO_3 was formed and how Mn^{4+} was stabilized throughout the slag need to be clarified. A promising approach would be to investigate phase relations (experimentally and theoretically) and to develop thermodynamic databases for a complex system in order to understand the processes taking place during solidification. Further investigations should indicate which slag modification should be performed to maximize EnAM yield.

Author Contributions: Conceptualization, A.S. and D.A.D.A.; methodology, A.S. and D.A.D.A.; validation, A.S. and D.A.D.A.; formal analysis, A.S. and D.A.D.A.; investigation, A.S., D.A.D.A., O.F. and T.S.; data curation, A.S. and D.A.D.A.; writing—original draft preparation, A.S., D.A.D.A., O.F. and T.S.; writing—review and editing, A.S., D.A.D.A., O.F. and T.S.; visualization, A.S. and D.A.D.A.; supervision, O.F. and T.S.; project administration, O.F. and T.S.; funding acquisition, O.F. and T.S. All authors have read and agreed to the published version of the manuscript.

Funding: This research was funded by the Open Access Publishing Fund of Clausthal University of Technology and the German Research Foundation as part of the priority program: Engineered Artificial Minerals (EnAM)—a geometallurgical tool for the recovery of critical elements from waste streams (SPP 2315, ProjNo. 470309740 and 470392360).

Data Availability Statement: The data presented in this study are available on request from the corresponding author.

Acknowledgments: We acknowledge the support by Open Access Publishing Fund of Clausthal University of Technology.

Conflicts of Interest: The funders had no role in the design of the study; in the collection, analyses, or interpretation of data; in the writing of the manuscript; or in the decision to publish the results.

References

1. Brückner, L.; Frank, J.; Elwert, T. Industrial Recycling of Lithium-Ion Batteries—A Critical Review of Metallurgical Process Routes. *Metals* **2020**, *10*, 1107. [CrossRef]
2. European Commission. Directorate General for Internal Market, Industry, Entrepreneurship and SMEs. In Study on the EU's List of Critical Raw Materials (2020): Final Report; Publications Office, Luxembourg 2020. Available online: https://data.europa.eu/doi/10.2873/11619 (accessed on 20 December 2023).
3. Bae, H.; Kim, Y. Technologies of lithium recycling from waste lithium ion batteries: A review. *Mater. Adv.* **2021**, *2*, 3234–3250. [CrossRef]
4. Ma, X.; Azhari, L.; Wang, Y. Li-ion battery recycling challenges. *Chem* **2021**, *7*, 2843–2847. [CrossRef]
5. U.S. Geological Survey. *Data Release for Mineral Commodity Summaries 2023*; U.S. Geological Survey: Reston, VA, USA, 2023.
6. Baum, Z.J.; Bird, R.E.; Yu, X.; Ma, J. Lithium-Ion Battery Recycling—Overview of Techniques and Trends. *ACS Energy Lett.* **2022**, *7*, 712–719. [CrossRef]
7. Sommerfeld, M.; Vonderstein, C.; Dertmann, C.; Klimko, J.; Oráč, D.; Miškufová, A.; Havlík, T.; Friedrich, A. Combined Pyro- and Hydrometallurgical Approach to Recycle Pyrolyzed Lithium-Ion Battery Black Mass Part 1: Production of Lithium Concentrates in an Electric Arc Furnace. *Metals* **2020**, *10*, 1069. [CrossRef]
8. Schnickmann, A.; Hampel, S.; Schirmer, T.; Fittschen, U.E.A. Formation of Lithium-Manganates in a Complex Slag System Consisting of Li_2O-MgO-Al_2O_3-SiO_2-CaO-MnO—A First Survey. *Metals* **2023**, *13*, 2006. [CrossRef]
9. Elwert, T.; Goldmann, D.; Schirmer, T.; Strauß, K. Recycling von Li-Ionen-Traktionsbatterien–Das Projekt LiBRi. *Recycl. Rohst.* **2012**, *5*, 679e690.
10. Schirmer, T.; Qiu, H.; Li, H.; Goldmann, D.; Fischlschweiger, M. Li-Distribution in Compounds of the Li_2O-MgO-Al_2O_3-SiO_2-CaO System—A First Survey. *Metals* **2020**, *10*, 1633. [CrossRef]
11. Pal, S.; Bandyopadhyay, A.K.; Mukherjee, S.; Samaddar, B.N.; Pal, P.G. $MgAl_2O_4$-γ-Al_2O_3 solid solution interaction: Mathematical framework and phase separation of α-Al_2O_3 at high temperature. *Bull. Mater. Sci.* **2011**, *34*, 859–864. [CrossRef]
12. Chatterjee, S.; Jung, I.-H. Critical evaluation and thermodynamic modeling of the Al–Mn–O (Al_2O_3–MnO–Mn_2O_3) system. *J. Eur. Ceram. Soc.* **2014**, *34*, 1611–1621. [CrossRef]
13. Ilatovskaia, M.; Fabrichnaya, O. Critical assessment and thermodynamic modeling of the Al-Mn-O system. *J. Alloys Compd.* **2021**, *884*, 161153. [CrossRef]
14. Kong, F.; Longo, R.C.; Park, M.-S.; Yoon, J.; Yeon, D.-H.; Park, J.-H.; Wang, W.-H.; Kc, S.; Doo, S.-G.; Cho, K. Ab initio study of doping effects on $LiMnO_2$ and Li_2MnO_3 cathode materials for Li-ion batteries. *J. Mater. Chem. A* **2015**, *3*, 8489–8500. [CrossRef]
15. Paulsen, J.M.; Dahn, J.R. Phase Diagram of Li−Mn−O Spinel in Air. *Chem. Mater.* **1999**, *11*, 3065–3079. [CrossRef]

16. Longo, R.C.; Kong, F.T.; Kc, S.; Park, M.S.; Yoon, J.; Yeon, D.-H.; Park, J.-H.; Doo, S.-G.; Cho, K. Phase stability of Li–Mn–O oxides as cathode materials for Li-ion batteries: Insights from ab initio calculations. *Phys. Chem. Chem. Phys.* **2014**, *16*, 11233–11242. [CrossRef] [PubMed]
17. Zhang, W.; Cupid, D.M.; Gotcu, P.; Chang, K.; Li, D.; Du, Y.; Seifert, H.J. High-Throughput Description of Infinite Composition–Structure–Property–Performance Relationships of Lithium–Manganese Oxide Spinel Cathodes. *Chem. Mater.* **2018**, *30*, 2287–2298. [CrossRef]
18. Müller, H.A.; Joshi, Y.; Hadjixenophontos, E.; Peter, C.; Csiszár, G.; Richter, G.; Schmitz, G. High capacity rock salt type $Li_2MnO_{3-\delta}$ thin film battery electrodes. *RSC Adv.* **2020**, *10*, 3636–3645. [CrossRef] [PubMed]
19. Mishra, G.; Jha, R.; Meshram, A.; Singh, K.K. A Review on Recycling of Lithium-Ion Batteries to Recover Critical Metals. *J. Environ. Chem. Eng.* **2022**, *10*, 108534. [CrossRef]
20. Konar, B.; Van Ende, M.-A.; Jung, I.-H. Critical Evaluation and Thermodynamic Optimization of the Li_2O-Al_2O_3 and Li_2O-MgO-Al_2O_3 Systems. *Metall. Mater. Trans. B* **2018**, *49*, 2917–2944. [CrossRef]
21. De Abreu, D.A.; Löffler, M.; Kriegel, M.J.; Fabrichnaya, O. Experimental investigation and thermodynamic modeling of the Li_2O-Al_2O_3 system. *J. Phase Equilibria Diffus.* **2024**, *45*, 36–55. [CrossRef]
22. Dilner, D.; Pavlyuchkov, D.; Zienert, T.; Kjellqvist, L.; Fabrichnaya, O. Thermodynamics of the Mg-Mn-O system—Modeling and heat capacity measurements. *J. Am. Ceram. Soc.* **2017**, *100*, 1661–1672. [CrossRef]
23. Zienert, T.; Fabrichnaya, O. Thermodynamic assessment and experiments in the system MgO–Al_2O_3. *Calphad* **2013**, *40*, 1–9. [CrossRef]
24. Blank, D.H.A.; Kruidhof, H.; Flokstra, J. Preparation of $YBa_2Cu_3O_{7-\delta}$ by citrate synthesis and pyrolysis. *J. Phys. D Appl. Phys.* **1988**, *21*, 226–227. [CrossRef]
25. Ehi-Eromosele, C.O.; Ajayi, S.O.; Onwucha, C.N. Influence of Fuels in the Sol-Gel Combustion Synthesis of Li_2MnO_3 Positive Electrode Material for Li-Ion Battery. *Mater. Chem. Phys.* **2021**, *259*, 124055. [CrossRef]
26. Downs, R.T.; Hall-Wallace, M. The American Mineralogist crystal structure database. *Am. Mineral.* **2003**, *88*, 247–250.
27. Gates-Rector, S.; Blanton, T. The Powder Diffraction File: A quality materials characterization database. *Powder Diffr.* **2019**, *34*, 352–360. [CrossRef]
28. Jercinovic, M.J.; Williams, M.L.; Allaz, J.; Donovan, J.J. Trace analysis in EPMA. *IOP Conf. Ser. Mater. Sci. Eng.* **2012**, *32*, 012012. [CrossRef]
29. Merlet, C. Quantitative Electron Probe Microanalysis: New Accurate Φ(pz) Description. In *Electron Microbeam Analysis*; Springer: Berlin/Heidelberg, Germany, 1992; pp. 107–115.
30. Schirmer, T. Stoichiometric Calculation of Lithium-Containing Phases Based on Spatially Resolved X-ray Analysis and Virtual Compounds. *Adv. X-ray Anal.* **2022**, *65*.
31. Shannon, R.D. Revised effective ionic radii and systematic studies of interatomic distances in halides and chalcogenides. *Acta Cryst. A* **1976**, *32*, 751–767. [CrossRef]
32. Tarascon, J.M.; McKinnon, W.R.; Coowar, F.; Bowmer, T.N.; Amatucci, G.; Guyomard, D. Synthesis Conditions and Oxygen Stoichiometry Effects on Li Insertion into the Spinel $LiMn_2O_4$. *J. Electrochem. Soc.* **1994**, *141*, 1421–1431. [CrossRef]
33. Yu, F.-D.; Wang, Z.-B.; Chen, F.; Wu, J.; Zhang, X.-G.; Gu, D.-M. Crystal structure and multicomponent effects in Li1+xMn2−x−yAlyO4 cathode materials for Li-ion batteries. *J. Power Sources* **2014**, *262*, 104–111. [CrossRef]
34. Luo, C.; Martin, M. Stability and defect structure of spinels $Li_{1+x}Mn_{2-x}O_{4-\delta}$: I. In situ investigations on the stability field of the spinel phase. *J. Mater. Sci.* **2007**, *42*, 1955–1964. [CrossRef]
35. Ilyushechkin, A.; Kondratiev, A. Viscosity of Slags with Solids: The Effect of Solids Morphology and Concentration. *J. Rheol.* **2019**, *63*, 719–733. [CrossRef]
36. Park, J.H.; Todoroki, H. Control of MgO·Al_2O_3 Spinel Inclusions in Stainless Steels. *ISIJ Int.* **2010**, *50*, 1333–1346. [CrossRef]
37. Nagata, K.; Sasabe, M. Permeability Coefficient of Oxygen in Molten Slags and Its Mechanisms. *ISIJ Int.* **2020**, *60*, 1872–1877. [CrossRef]